

# Light Field Saliency Detection with Deep Convolutional Networks

Jun Zhang, Yamei Liu, Shengping Zhang, Ronald Poppe, and Meng Wang

**Abstract**—CNN-based methods have been proven to work well for saliency detection on RGB images owing to the outstanding feature representation abilities of CNNs. However, their performance will degrade when detecting multiple saliency regions in highly cluttered or similar backgrounds. To address these problems, in this paper we resort to light field imaging, which records the color intensity of each pixel as well as the directions of incoming light rays, and thus can improve performance for saliency detection owing to the usage of both spatial and angular patterns encoded in light field images. However, it is not trivial to use CNN-based methods for saliency detection on light field images because these methods are not specifically designed for processing light field inputs and current light field datasets are not sufficiently large to train CNNs. To overcome these issues, we first present a new Lytro Illum dataset, which contains 640 light fields and their corresponding micro-lens images, central-viewing images as well as ground-truth saliency maps. Comparing to the current light field saliency datasets [1], [2], the new dataset is larger, of higher quality, contains more variations and more types of light field inputs, which is suitable for training deeper networks as well as better benchmarking algorithms. Furthermore, we propose a novel end-to-end CNN-based framework for light field saliency detection as well as its several variants. We systematically study the impact of different variants and compare light field saliency with regular 2D saliency on the performance of the proposed network. We also conduct extensive experimental comparisons, which indicate that our network significantly outperforms state-of-the-art methods on the proposed dataset and has desired generalization abilities on other existing datasets.

## I. INTRODUCTION

**L**IGHT field imaging [3] not only captures the color intensity of each pixel but also the directions of all incoming light rays. The directional information inherent in a light field implicitly defines the geometry of the observed scene [4]. In recent years, with a micro-lens array inserted between the main lens and the photosensor, commercial and industrial light field cameras such as Lytro [5] and Raytrix [6] have taken light field imaging into a new era. The obtained light field can be represented by 4D parameterization  $(u, v, x, y)$  [7], where  $uv$  denotes the viewpoint plane and  $xy$  denotes the image plane, as shown in Figures 1(a) and (c). The 4D light field can be further converted into multiple 2D light field images, such as multi-view sub-aperture images [7], micro-lens images [8], and

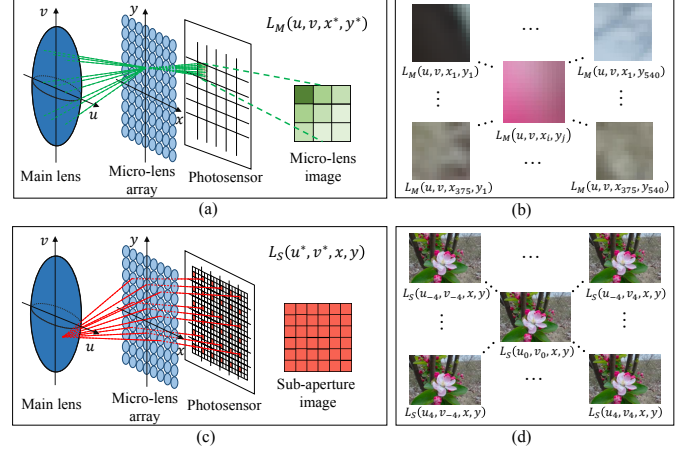


Fig. 1. Illustrations of light field representations. (a) Micro-lens image representation with the given location  $(x^*, y^*)$ . (b) Micro-lens images at sampled spatial locations. (c) Sub-aperture image representation with the given viewpoint  $(u^*, v^*)$ . (d) Sub-aperture images at sampled viewpoints, where  $(u_0, v_0)$  represents the central viewpoint.

epipolar plane images (EPIs) [9]. These light field images have been exploited to improve the performance of many applications, such as material recognition [10], face recognition [11], [12], depth estimation [13]–[17], super-resolution [9], [18], [19] and saliency detection [1], [2], [20], [21].

This paper studies the new problem of saliency detection on light field images. Previous attempts [1], [2], [20], [21] focus on developing hand-crafted light field features at the superpixel level by utilizing heterogeneous types of light field images (e.g., color, depth, focusness, or flow). However, these methods strongly rely on low-level cues and are incapable to extract high-level semantic concepts, which makes them unable to handle highly cluttered backgrounds or predict uniform regions inside salient objects.

In recent years, convolutional neural networks (CNNs) have been successfully used to learn an implicit relation between pixels and salience on RGB images [22]–[28]. These CNN-based methods have often combined with object proposal [22], post-processing [23], contextual features [24], [25], attention models [26], [27], as well as recurrent structure [28]. Although these approaches achieve improved performance on benchmark datasets, they often suffer from complex network architectures. Besides, geometric constraints are not fully exploited owing to the limited information in RGB images, which have been shown to be beneficial in saliency detection [29], [30].

In this paper, we propose a novel method to predict the salience of a given light field by utilizing deep learning

J. Zhang, Y. Liu, and M. Wang are with the School of Computer Science and Information Engineering, Hefei University of Technology, Hefei, Anhui, 230601 China.

S. Zhang is with the School of Computer Science and Technology, Harbin Institute of Technology, Weihai, Shandong, 264209 China.

R. Poppe is with the Department of Information and Computing Sciences, Utrecht University, 3584 CC Utrecht Netherlands.

Corresponding author: Jun Zhang (e-mail: zhangjun1126@gmail.com)

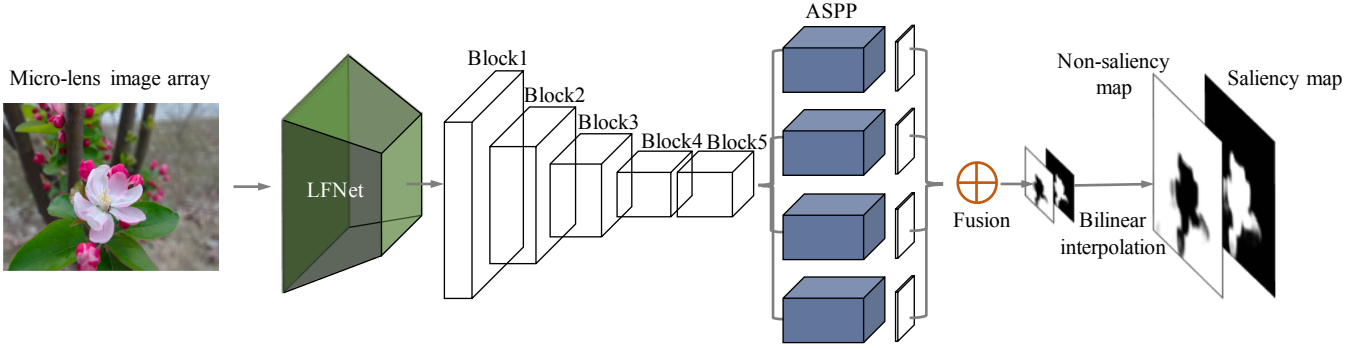


Fig. 2. Architecture of our network. The LFNet converts the micro-lens image array of light fields into feature maps, which are followed by a modified DeepLab-v2 backbone model.

technologies. Even with the emergence of CNNs on RGB images, there are still three key issues for saliency detection on light field images: (1) The RGB datasets [31]–[33] are not sufficient to address significant variations in illumination, scale, background clutter, among others. (2) Previous light field saliency datasets LFSD [1] and HFUT-Lytro [2] include only 100 and 255 light fields captured by the first-generation Lytro cameras, respectively, so they are not large enough to train deep convolutional networks without severely overfitting. In addition, the unavailability of multi-views in the LFSD dataset and the color distortion of the sub-aperture images in the HFUT-Lytro dataset are not enough to evaluate existing methods. (3) The adoption of CNN-based architectures to light field saliency detection is not trivial because the existing CNNs for 2D images are not sufficient to represent 4D light field data. Thus, novel architectures must be developed for saliency detection on light field images.

Based on the aforementioned issues, we introduce a comprehensive, realistic and challenging benchmark dataset for light field saliency detection. Using a Lytro Illum camera, we collect 640 light fields with significant variations in terms of size, texture, background clutter and illumination, *etc.* Comparing to the low quality and limited angular resolutions of light fields in previous datasets [1], [2], we provide a high-quality micro-lens image array for each light field, which contains multiple viewpoints for each spatial location. The micro-lens image array is first used as input for light field saliency detection. Then, we annotate per-pixel ground truth for each central viewing image.

To explore spatial and multi-view properties of light fields for saliency detection, we further propose a novel deep convolutional network based on the modified DeepLab-v2 model [34] as well as several subnetwork variants (LFNet) specifically designed for light field images. Figure 2 provides an overview of the proposed network. The LFNet processes the micro-lens image array by learning angular convolutional kernels, and is followed by five convolutional blocks for encoding spatial features, atrous spatial pyramid pooling (ASPP) to capture multi-scale information, a score layer with  $1 \times 1$  convolution to generate the probability value of salience/non-salience, a sum-pooling layer for score fusion, and a final up-sampling layer with bilinear interpolation to guarantee that

the predicted map and the ground truth map have the same spatial resolution. In addition, dropout and data augmentation are applied during training to prevent overfitting.

Our contributions are summarized as follows.

- We construct a new light field dataset for saliency detection, which comprises of 640 high-quality light fields and the corresponding per-pixel ground-truth saliency maps. To our knowledge, this is the largest light field dataset so far that enables efficient deep network training for saliency detection, and address new challenges in saliency detection such as inconsistent illumination and small salient objects in the cluttered or similar background.
- We propose an end-to-end deep convolutional network for predicting saliency on light field images. In particular, we propose several novel architectures applied on the micro-lens image arrays to learn multi-view information. To the best of our knowledge, no work has been reported in the literature on employing deep learning techniques for light field saliency detection.
- We provide an analysis on the proposed architecture variants specifically designed for light-field inputs. We also compare our best-performing architecture with the 2D model using the central viewing image from quantitative and qualitative prediction results as well as by visualizing learned weights and feature maps of different layers. Our experiments suggest that the benefits of light field multi-view information in saliency detection. Moreover, we show that our network strongly outperforms state-of-the-art methods on the proposed dataset and generalizes well to other existing datasets. It acts as an important baseline for future work in light field saliency detection.

## II. RELATED WORK

### A. Light field datasets for saliency detection

There are only two existing datasets designed for light field saliency detection, which are constructed using Lytro’s first-generation cameras. The first Light Field Saliency Database (LFSD) [1] contains 100 light fields with  $360 \times 360$  spatial resolution, in which a rough focal stack and a central viewing image are provided for each light field. The image in this dataset usually has one foreground salient object in the high

color contrast background. The limited complexity of the dataset is not sufficient to address the variety of challenges for saliency detection when using a light field camera, such as illumination variations and small objects in the similar or cluttered background, *etc.* Later, Zhang *et al.* [2] proposed the HFUT-Lytro dataset, which consists of 255 light fields with complex backgrounds and multiple salient objects. Each light field has a  $7 \times 7$  angular resolution and  $328 \times 328$  pixels of spatial resolution. However, the color channels in their sub-aperture images are distorted owing to the under-sampling during decoding [35]. Moreover, we can know that there is a lack of larger light field datasets for saliency detection in prior works. In this work, we use a Lytro Illum camera to build a larger, higher-quality and challenging saliency dataset by capturing larger variations in illuminance, scale, position, which is an important step towards deep learning based light field research. We also generate the micro-lens image array for each light field, which is not provided in previous datasets.

### B. Saliency detection on light field images

Previous methods on light field saliency detection mainly rely on superpixel-level hand-crafted features [1], [2], [20], [21]. The pioneering work [1] shows the feasibility of detecting salient regions using all-in-focus images and focal stacks from light fields. Zhang *et al.* [20] explored the light field depth cue in saliency detection, and further computed light field flow fields over focal slices and multi-view sub-aperture images to capture depth contrast [2]. In [21], a dictionary learning based method is presented to combine various light field features using a sparse coding framework. Notably, these approaches share the assumption that dissimilarities between image regions imply salient cues. In addition, some of them [2], [20], [21] also utilize refinement strategies to enforce neighboring constraints for saliency optimization. In contrast to the above methods, we propose a deep convolutional network by learning efficient angular kernels without extra refinement on the upsampled image.

### C. Deep learning for saliency prediction

More recently, remarkable advances in deep learning drive research towards the use of CNNs for saliency detection [22]–[28]. Different from conventional learning-based methods, CNNs can directly learn an end-to-end mapping between 2D images and saliency maps. Since the task is closely related to pixel-wise image classification, most works have built upon the most successful architectures for image recognition on the ImageNet dataset [36], often initializing their networks with the VGG network [37]. For example, several methods [24], [25] directly use CNNs to learn effective contextual features and combine them to infer saliency. Some other methods [38], [39] extract features at multiple scales and generate saliency maps in a fully convolutional way. Recently, attention models [26], [27] have been introduced into saliency detection to mimic the visual attention mechanism of focusing on informative regions in visual scenes. Another direction for improving the quality of the saliency maps is the use of recurrent structure [28], which mainly serves as a refinement to correct previous errors.

Although deep CNNs have achieved great success in saliency detection, none of them addresses problems in the 4D light field. Directly applying the existing network architectures to light field images would not be appropriate because a standard network is not particularly good at capturing viewpoint changes in light fields. Our work can be viewed as the first piece of work that aims for light field saliency detection by developing end-to-end deep convolutional networks.

## III. THE LYTRO ILLUM SALIENCY DATASET

To train and evaluate our network for saliency detection, we collect a new light field dataset.

### A. Light field representation

There are various ways to represent the light field [7], [40], [41], we adopt the two-plane parameterization [7] to define the light field as a 4D function  $L(u, v, x, y)$ , where  $u \times v$  indicates the angular resolution and  $x \times y$  indicates the spatial resolution. As illustrated in Figures 1(a) and (b), a set of all incoming rays from the  $uv$  plane intersected with a given micro-lens location  $(x^*, y^*)$  produces a micro-lens image with multiple viewpoints  $L_M(u, v, x^*, y^*)$ . The micro-lens images over different locations can be arranged into a micro-lens image array. As shown in Figures 1(c) and (d), all the micro-lens regions on the  $xy$  plane receive the incoming rays from a given angular position  $(u^*, v^*)$ , which produces a sub-aperture image with all locations  $L_S(u^*, v^*, x, y)$ . The central viewing image is formed by the rays passed through the main lens optical center ( $u = u_0, v = v_0$ ). Since the sub-aperture images contain optical distortions caused by the light rays passed through the lens [42], [43], in this paper, we build our network based on the micro-lens images, which have been shown advantages over the sub-aperture images for scene reconstruction [44].

### B. Dataset construction

Figure 3 illustrates the procedure of our light field dataset construction. First, a set of 4D light fields are obtained by using a Lytro Illum camera shown in Figure 3(a). Second, we use Lytro Power Tools (LPT) [45] to decode light fields from raw 4D data to 2D sub-aperture images so that each light field has the spatial resolution of  $540 \times 375$  and the angular resolution of  $14 \times 14$ . To reach a compromise on the training time and the detection accuracy, we sample  $9 \times 9$  viewpoints from each light field to generate new sub-aperture images, as shown in Figure 3(b). Third, we generate a micro-lens image by sampling the same spatial location from each sub-aperture image, which further produces a micro-lens image array of size  $4860 \times 3375$  shown in Figure 3(c). The red highlight region indicates one pixel with  $9 \times 9$  observation viewpoints in Figure 3(c), comparing to one pixel only with the central view in Figure 3(d). We initially collect 800 light fields and manually annotate the per-pixel ground-truth label for each central viewing image. To reduce label inconsistency, each image is annotated by five independent annotators. We only regard a pixel as saliency if it is verified by at least three



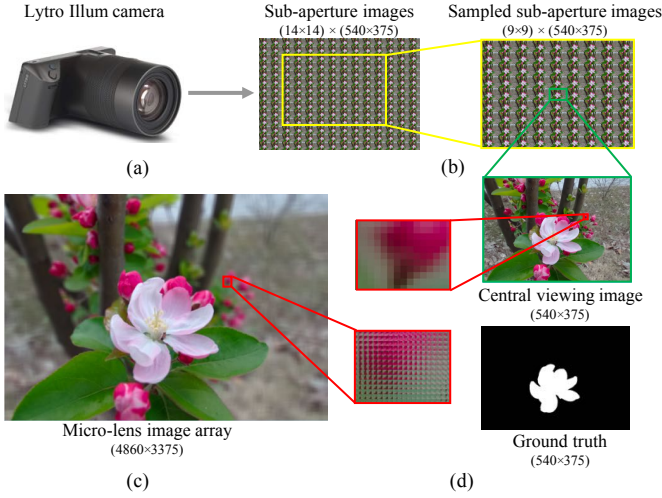


Fig. 3. Flowchart of the dataset construction. (a) Lytro Illum camera. (b) Sub-aperture images. (c) Micro-lens image array. (d) The ground-truth map for the central viewing image.



Fig. 4. Some representative central viewing images (top) and their corresponding ground-truth saliency maps (bottom) from the proposed Lytro Illum dataset.

annotators. In the end, our new dataset contains 640 light fields with 81 views.

Figure 4 shows eight examples of central viewing images and their corresponding ground-truth saliency maps in the proposed dataset. We can see that there are significant variations in illumination, spatial distribution, scale and background of salient objects. Besides, there are multiple regions for some of saliency annotations.

#### IV. LIGHT FIELD SALIENCY NETWORK

We propose an end-to-end deep convolutional network framework for light field saliency detection as shown in Figure 2. Based on the micro-lens image array, LFNet is designed to transfer the light field inputs to feature maps in different ways. Then, the feature maps are fed to the modified DeepLab-v2 [34] to predict saliency maps.

##### A. Backbone model

We formulate light field saliency detection as a binary pixel labeling problem. Saliency detection and semantic segmentation are closely related because both of them are pixel-wise labeling tasks and require low-level cues as well as high-level semantic information. Inspired by previous literature in semantic segmentation [34], [46], [47], we design our backbone model based on DeepLab [47], which is a variant of FCNs [46] modified from the VGG-16 network [37]. There are several variants of DeepLab [34], [48], [49]. In this work, we mainly use DeepLab-v2 [34], which introduces ASPP to capture

multi-scale information and long-range spatial dependencies among image units.

The modified network is composed of five convolutional (*conv*) blocks, each of which are divided into convolutions followed by a ReLU. A max-pooling layer is connected after the top *conv* layer of each *conv* block. The ASPP is applied on top of “Block5”, which consists of four branches with atrous rates ( $r = \{6, 12, 18, 24\}$ ). Each branch contains one  $3 \times 3$  convolution and one  $1 \times 1$  convolution. The resulting features from all the branches are then passed through another  $1 \times 1$  convolution and summed to generate the final score value. The network further employs bilinear interpolation to upsample the fused score map to the original resolution of the central viewing image, which produces the saliency prediction at the pixel level. In addition, we add dropout to all the *conv* layers of the five blocks to avoid overfitting and set the  $1 \times 1$  *conv* layer with 2 channels after ASPP to produce saliency and non-saliency score maps. The detailed architecture is illustrated in Figure 5.

##### B. LFNet variants

Our network is essentially a modified DeepLab-v2 network augmented with a light field input process. We add a light field module, which we refer as LFNet shown in Figure 2. We convert the 4D light field into a 2D micro-lens image array before feeding it to the network. In particular, we propose three different LFNet variant architectures to process the light field micro-lens image arrays before “Block1” of the backbone model, in which convolutional methods with kernel sizes, stride size and sampled viewpoints are all tailored to light field inputs to capture angular changes in light fields. The proposed LFNet architectures are shown in Figure 6. In the following section, we present the architectures of the variants in detail.

1) *LFNet-9 × 9*: As described in Section III-B, each micro-lens image has  $9 \times 9$  viewpoints and can be considered as one of the pixel locations. The spatial resolution is  $540 \times 375$  thus the size of the whole micro-lens image array is  $4860 \times 3375$ . In this architecture, we design angular convolutional kernels across all the viewpoint directions, as shown in Figure 6(a). The kernel size share the same angular resolution of one micro-lens image, and the number of kernels and the stride size are set to extract angular features for each micro-lens image. Specifically, we propose 64 angular kernels, each of which is a  $9 \times 9$  filter. The stride of convolution operations is 9, which leads to  $540 \times 375 \times 64$  feature maps. Each point on the feature map can be considered as being captured by the 81 lenslets. These kernels differ from common convolutional kernels applied on 2D images in that they only detect the angular changes in the micro-lens image array. This architecture directly learns the angular information from light field images, and thus is expected to distinguish salient foregrounds and backgrounds with similar colors or textures.

2) *LFNet-3 × 3*: Motivated by the effectiveness of the smaller kernels in VGG-16 [37] and Inception v2 [48], we replace the  $9 \times 9$  convolution in LFNet- $9 \times 9$  with two layers of  $3 \times 3$  convolution (stride= 3) shown in Figure 6(b), which increases the number of parameters but enhances the network nonlinearity.



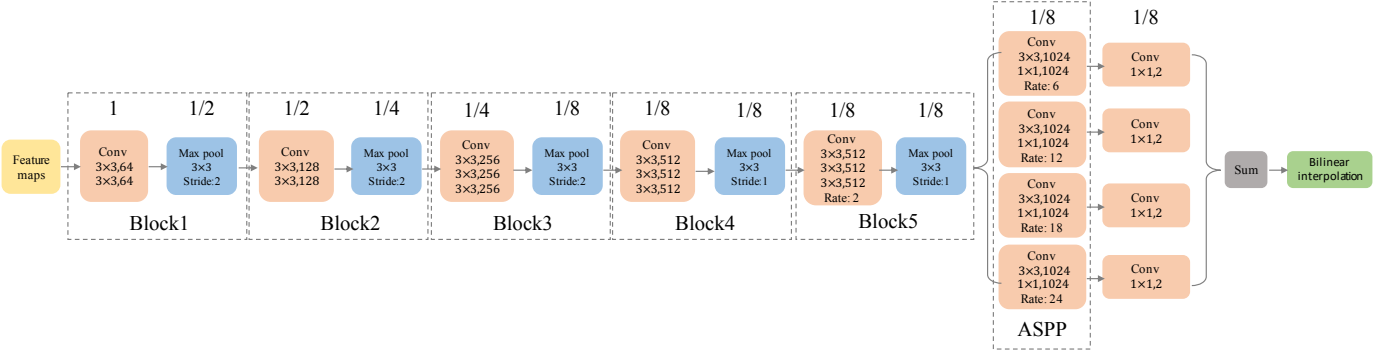


Fig. 5. Network structure of the backbone model based on DeepLab-v2 [34]. The reduction in resolution is shown on the top of each box.

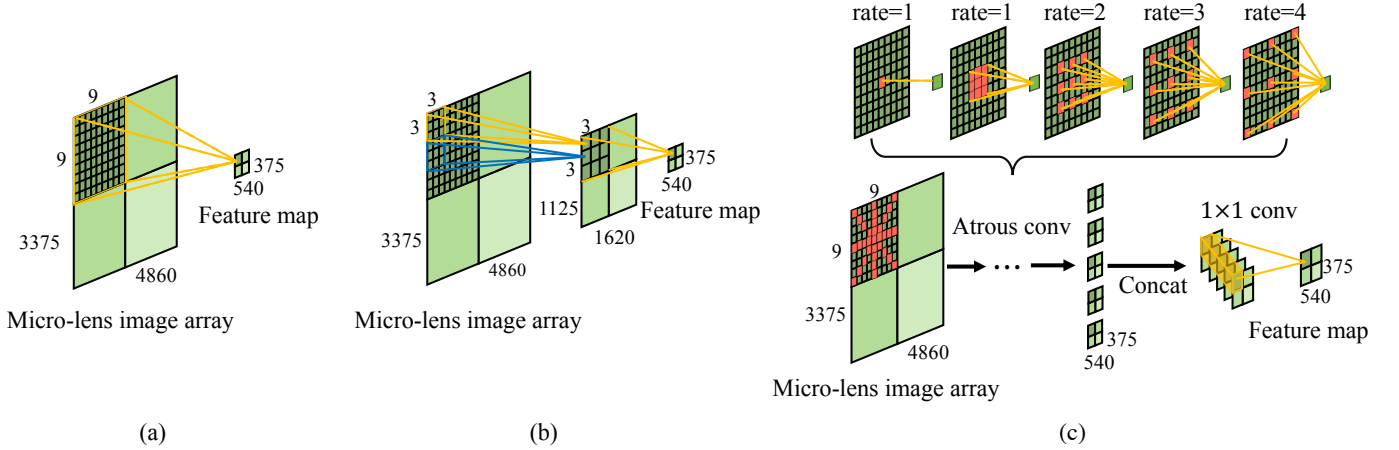


Fig. 6. Architectures of the proposed LFNet. (a) LFNet-9  $\times$  9. (b) LFNet-3  $\times$  3. (c) LFNet-star shaped. The selected viewpoints are highlighted in red.

3) *LFNet-star shaped*: We design atrous angular convolutional kernels to capture long-range angular features. The atrous rates are set to sample representative viewpoint directions. Different from LFNet-9  $\times$  9, we select star-shaped viewpoints (*i.e.* four directions  $\theta = \{0^\circ, 45^\circ, 90^\circ, 135^\circ\}$ ) from each micro-lens image. To implement viewpoint sampling and angular filtering, we use atrous convolution with five atrous rates, as shown in Figure 6(c). The resulting feature maps are concatenated and combined using  $1 \times 1$  convolutions for later processing. In fact, it has been shown that using selected angular directions is beneficial in the context of depth estimation [15], [50].

## V. EXPERIMENTAL RESULTS

### A. Settings

1) *Implementation and training*: The computational environment has an Intel i7-6700K CPU@4.00GHz, a 15GB RAM, and an NVIDIA GTX1080Ti GPU. We trained our network using the Caffe library [51] with the maximum iteration step of 160K. We initialize the backbone model with DeepLab-v2 [34] pre-trained on the PASCAL VOC 2012 segmentation benchmark [52]. The newly added *conv* layers in LFNet, the first layer of “Block1”, and the score layer are initialized using the Xavier algorithm [53]. The whole network is trained end-to-end using the stochastic gradient descent

(SGD) algorithm. To leverage the training time and the image size, we use a single image batch size. The momentum and the weight decay are set to 0.9 and 0.0005, respectively. The base learning rate is initialized as 0.01 for the newly added *conv* layers in LFNet and the first layer of “Block1”, while 0.001 with the “poly” decay policy for the remaining layers. A dropout layer with probabilities  $p = [0.1, 0.1, 0.2, 0.2, 0.3, 0.5]$  is applied after *conv* layers for “Block1”–“Block5” and ASPP, respectively.

We use the softmax loss function defined as

$$L = -\frac{1}{W \times H} \sum_{i=1}^W \sum_{j=1}^H \log \frac{e^{z_{i,j}^{y_{i,j}}}}{e^{z_{i,j}^0} + e^{z_{i,j}^1}} \quad (1)$$

where  $W$  and  $H$  indicate the width and height of an image,  $z_{i,j}^0$  and  $z_{i,j}^1$  are the last two activation values of the pixel  $(i, j)$ ,  $y_{i,j}$  is the ground-truth label of the pixel  $(i, j)$ . Note that  $y_{i,j}$  is 1 only when pixel  $(i, j)$  is salient. Our code and dataset are available at <https://github.com/pencilzhang/LFNet-light-field-saliency-net.git>.

2) *Datasets*: Three datasets are used for benchmarking: the proposed Lytro Illum dataset, the HFUT-Lytr dataset [2], and the LFSD dataset [1]. Our network is trained and evaluated on the proposed Lytro Illum dataset using a five-fold cross-validation. The trained model is further tested on the other two datasets to evaluate the generalization ability of our network. Note that the unavailable viewpoints in the LFSD dataset and

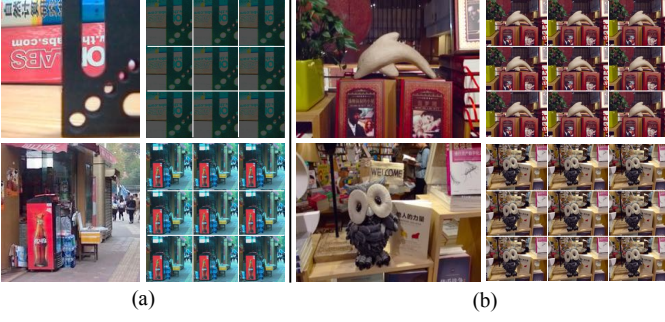


Fig. 7. Light field image examples in (a) the HFUT-Lytro dataset and (b) the proposed Lytro-illum dataset. The central viewing image (left) and nine randomly sampled sub-aperture images (right) are shown for each example.

the color distortion of sub-aperture images in the HFUT-Lytro dataset (see examples in Figure 7 for visual comparison) are too low to evaluate our method. To apply the trained model on the two datasets, we pad the angular resolutions to  $9 \times 9$  using the central viewpoint.

3) *Data augmentation*: In order to obtain more training data to achieve good performance without overfitting, we augment the training data aggressively on-the-fly. To facilitate this augmentation, we use geometric transformations (*i.e.* rotation, flipping and cropping), changes in brightness, contrast, and chroma as well as additive Gaussian noise. Specifically, we rotate the micro-lens image array 90, 180, and 270 degrees, and perform horizontal and vertical flipping. To change the relative position of the saliency region in the image, we randomly crop two subimages of  $3519 \times 2907$  size from the micro-lens image array. Then for one subimage and the image arrays with 0, 90, and 180 degrees of rotation, we adjust the brightness by multiplying all pixels by 1.5 and 0.6, respectively, and both chroma and contrast by the multiplication factor 1.7. Finally, we add the zero-mean Gaussian noise with variance of 0.01 to all images. In total, we expand the micro-lens image array by 48 ( $(4 \times 4 + 8) \times 2$ ) such that the whole training dataset is increased from 512 to 24,576.

4) *Evaluation metrics*: We adopt five metrics to evaluate our network. The first one is precision-recall (PR) curve. Specifically, saliency maps are first binarized and then compared with the ground truths under varying thresholds. The second metric is  $F_\beta$ -measure, which considers both precision and recall

$$F_\beta = \frac{(1 + \beta^2) \text{Precision} \cdot \text{Recall}}{\beta^2 \cdot \text{Precision} + \text{Recall}} \quad (2)$$

where  $\beta^2$  is set to 0.3 as suggested in [31]. The third metric is Average Precision (AP), which is computed by averaging the precision values at evenly spaced recall levels. The fourth metric is Mean Absolute Error (MAE), which computes the average absolute per-pixel difference between the predicted map and the corresponding ground-truth. Additionally, to amend several limitations of the above four metrics, such as interpolation flaw for AP, dependency flaw for PR curve and  $F_\beta$ -measure, and equal-importance flaw for all the metrics, as

TABLE I  
QUANTITATIVE RESULTS ON THE PROPOSED LYTRO ILLUM DATASET

Method	F-measure	WF-measure	MAE	AP
LFNet-star shaped	0.8045	0.7426	0.0555	0.9120
LFNet- $3 \times 3$	0.8066	0.7471	0.0562	0.9118
LFNet- $9 \times 9$	<b>0.8116</b>	<b>0.7540</b>	<b>0.0551</b>	<b>0.9124</b>

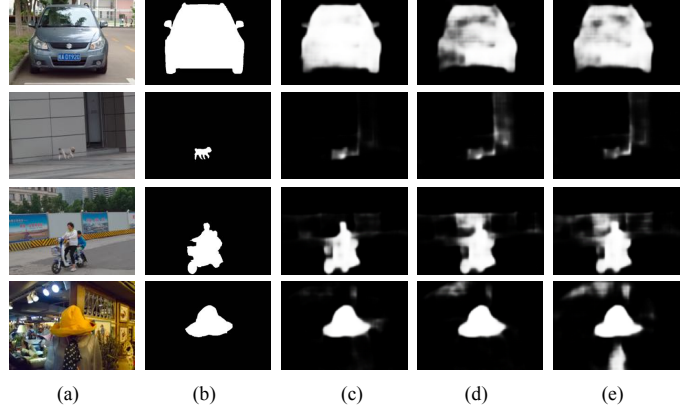


Fig. 8. Visual comparison of different LFNet variants. (a) Central viewing images. (b) Ground-truth maps. (c) LFNet- $9 \times 9$ . (d) LFNet- $3 \times 3$ . (e) LFNet-star shaped.

suggested in [54], we use weighted  $F_\beta^w$  (WF)-measure based on weighted precision and recall as the fifth metric

$$F_\beta^w = \frac{(1 + \beta^2) \text{Precision}^w \cdot \text{Recall}^w}{\beta^2 \cdot \text{Precision}^w + \text{Recall}^w} \quad (3)$$

where  $w$  is a weighting function based on the Euclidean distance to calculate the pixel importance from the ground-truth.

### B. Ablation Study

1) *LFNet variants*: We present a detailed performance comparison among different LFNet variant architectures on the proposed Lytro Illum dataset: LFNet- $9 \times 9$ , LFNet- $3 \times 3$ , and LFNet-star shaped. As described in Section IV-B, these variants only differ in the convolution operations applied on their light field inputs. The quantitative results of the comparison are shown in Tables I, from which we can see that the LFNet- $9 \times 9$  architecture achieves the best performance for all metrics on the proposed dataset. We hypothesize that treating every micro-lens image as a whole and applying the angular kernels that have the same size with the angular resolution of the light field can help exploit the multi-view information in the micro-lens image array. The detection performances of two other variants are reduced owing to that more parameters would make the network learning difficult.

Figure 8 presents qualitative results of all variants. As illustrated in the figure, we can see that these variants can separate the most salient regions from the similar or cluttered background. Comparing to other variants, LFNet- $9 \times 9$  outputs cleaner and more consistent predictions for the regions with specular reflection (row 1), the small salient object (row 2), and the similar foreground and background (rows 2 and 3).

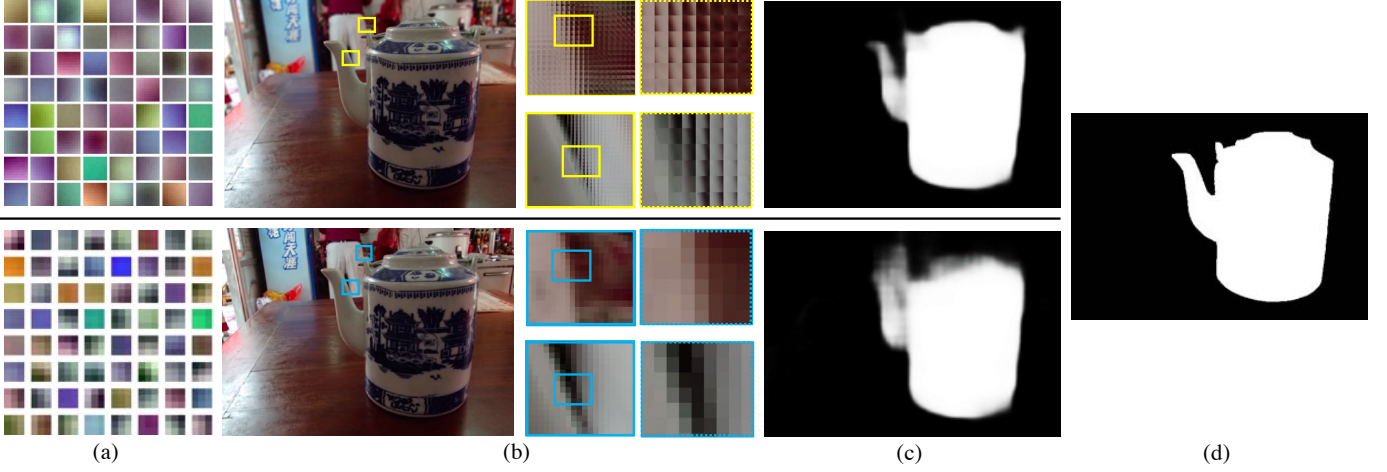


Fig. 9. Visualization comparison between LFNet- $9 \times 9$  (top) and 2D-central view (bottom). (a) Visualization of the first *conv* layers. (b) Light field input with its highlighted regions. (c) Saliency predictions. (d) Ground-truth maps.

TABLE II  
QUANTITATIVE COMPARISON BETWEEN LFNET- $9 \times 9$  AND 2D-CENTRAL VIEW ON THE PROPOSED LYTRO ILLUM DATASET

Method	F-measure	WF-measure	MAE	AP
LFNet- $9 \times 9$	<b>0.8116</b>	<b>0.7540</b>	<b>0.0551</b>	<b>0.9124</b>
2D-central view	0.8056	0.7446	0.0597	0.9016

TABLE III  
EFFECTS OF THE ANGULAR RESOLUTION ON THE PROPOSED DATASET

Angular resolution	F-measure	WF-measure	MAE	AP
$7 \times 7$	0.8018	0.7406	0.0567	<b>0.9135</b>
$9 \times 9$	<b>0.8116</b>	<b>0.7540</b>	<b>0.0551</b>	0.9124
$11 \times 11$	0.8006	0.7392	0.0567	0.9109

Moreover, we can see that LFNet- $9 \times 9$  better predicts salient regions without being highly affected by the light source (row 4) that is not addressed by existing datasets. These results demonstrate that the proposed network variants are likely to extract potential depth cues by learning angular changes, which are helpful to saliency detection. The kernels with the same size of the angular resolution show better capability in depth discrimination.

2) *4D light field saliency vs. 2D saliency*: To further delve into the difference between regular image saliency and light field saliency, we present some important properties of light field features that can better facilitate saliency detection. We compare 4D light field saliency (the best-performing LFNet- $9 \times 9$  model) with 2D model using the central viewing image as input (2D-central view). The quantitative results are shown in Tables II. We found that light field saliency detector with multi-views turns out to perform better than the 2D detector only with the central view.

To provide complementary insight of why light field saliency works, we visualize the weights of the first *conv* layers of LFNet- $9 \times 9$  and 2D-central view in Figure 9(a) to compare angular and spatial patterns. We can see that the learned weights from LFNet- $9 \times 9$  have noticeable changes in angular space, suggesting the viewpoint cue of light field data is well captured. The angular changes are also consistent with the viewpoint variations of micro-lens images, as shown in Figure 9(b). The results are attributed to the newly designed *conv* method in which the kernel size is the same as the angular resolution of the micro-lens image, the channel number equals to the number of viewpoints, and the stride size guarantees

angular features are extracted for each micro-lens image. Therefore, our 4D saliency detector produces more accurate saliency map than the 2D detector shown in Figure 9(c).

In addition, we show the feature maps obtained from the two models in Figure 10. It can be seen that different layers encode different types of features. Higher layers capture semantic concepts on the salient region, whereas lower layers encode more discriminative features for identifying the salient region. The proposed 4D saliency detector can well discriminate the white spout from the white pants, as shown in Figure 10(a). However, as illustrated in the Block1-conv1 and Block5 of Figure 10(b), most of the feature maps from the 2D detector have small or zero values that are not discriminative enough to separate the salient teacup from the pants. Thus the 2D detector produces features cluttered with background noise in the following ASPP and score fusion. More comparisons of saliency maps between the two models can be seen in Figure 11.

3) *Effect of the angular resolutions*: To show the effect of the angular resolutions in the network, we compare the performance of the LFNet- $9 \times 9$  architecture with varying number of viewpoints in Table III. Note we change the kernel size to stay the same with the angular resolution. The results are all converged with 160K iterations. From the table, we can see that the network using  $9 \times 9$  viewpoints shows the overall best performance. Increasing the angular resolution to  $11 \times 11$  cannot improve the performance, which can be explained by the fact that the viewing angles at the boundary are very oblique [55] and the narrow baseline of the light field camera leads to high viewing redundancy with higher angular



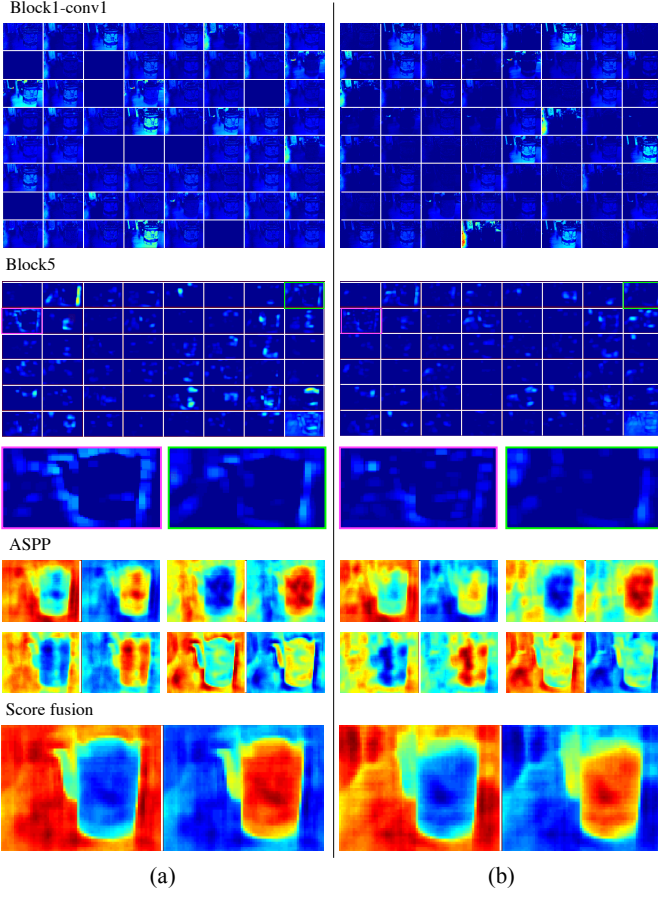


Fig. 10. Feature maps obtained from (a) LFNet-9  $\times$  9 and (b) 2D-central view from different layers. From top to bottom: the first *conv* features of Block1, Block5 output features, ASPP features with four atrous rates, and the score fusion maps via sum-pooling. For ASPP and sum fusion, the non-saliency and saliency scores are shown in the left and right subfigures, respectively.

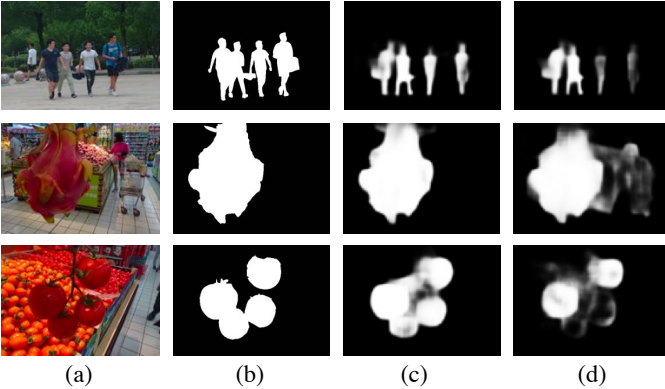


Fig. 11. Visual comparison of LFNet-9  $\times$  9 and 2D-central view. (a) Central viewing images. (b) Ground-truth maps. (c) LFNet-9  $\times$  9. (d) 2D-central view.

resolutions [7], [56].

4) *Overfitting issues*: Overfitting is a common problem related to training a CNN with limited data. In this section, we analyse the proposed network by introducing different strategies to handle overfitting: data augmentation (DG) and dropout. The results obtained from LFNet-9  $\times$  9 are shown in

TABLE IV  
QUANTITATIVE RESULTS ON THE PROPOSED LYTRO ILLUM DATASET. BOLD: BEST, UNDERLINE: SECOND BEST

Method	F-measure	WF-measure	MAE	AP
LFS [1]	0.6107	0.3596	0.1697	0.6193
WSC [21]	0.6451	<u>0.5945</u>	<u>0.1093</u>	0.5958
DILF [20]	0.6395	0.4844	0.1389	<u>0.6921</u>
Multi-cue [2]	<u>0.6648</u>	0.5420	0.1197	0.6593
LFNet-9 $\times$ 9	<b>0.8116</b>	<b>0.7540</b>	<b>0.0551</b>	<b>0.9124</b>

TABLE V  
QUANTITATIVE RESULTS ON THE HFUT-LYTRO DATASET. BOLD: BEST, UNDERLINE: SECOND BEST

Method	F-measure	WF-measure	MAE	AP
LFS [1]	0.4868	0.3023	0.2215	0.4718
WSC [21]	0.5552	0.5080	0.1454	0.4743
DILF [20]	0.5543	0.4468	0.1579	0.6221
Multi-cue [2]	<u>0.6135</u>	<u>0.5146</u>	0.1388	<u>0.6354</u>
LFNet-9 $\times$ 9	<b>0.6693</b>	<b>0.5998</b>	<b>0.1032</b>	<b>0.7324</b>

TABLE VI  
QUANTITATIVE RESULTS ON THE LFSD DATASET. BOLD: BEST, UNDERLINE: SECOND BEST

Method	F-measure	WF-measure	MAE	AP
LFS [1]	0.7525	0.5319	0.2072	0.8161
WSC [21]	0.7729	<u>0.7371</u>	0.1453	0.6832
DILF [20]	<u>0.8173</u>	0.6695	<u>0.1363</u>	<b>0.8787</b>
Multi-cue [2]	<b>0.8249</b>	0.7155	0.1503	<u>0.8625</u>
LFNet-9 $\times$ 9	0.8105	<b>0.7378</b>	<b>0.1164</b>	0.8561

Figure 12. Obviously, the network is overfitting with original training data as shown in Figure 12(a). As expected, both DG and dropout are crucial to minimize overfitting as shown in Figures 12(b)–(d). Figure 12(e) presents the corresponding PR curves. It can be seen that by increasing the amount and diversity of the data and the number of dropout between different layers with certain probabilities during training, the performance of the network increases as well.

### C. Comparison to state-of-the-arts

We compare our best performing model LFNet-9  $\times$  9 to four state-of-the-art methods: Multi-cue [2], DILF [20], WSC [21], and LFS [1]. The results are obtained using the authors' implementations. Tables IV–VI and Figure 13 show quantitative results on three datasets.

Overallly speaking, our approach outperforms other methods on three datasets without any post-processing for refinement, which proves the advantage of the proposed deep convolutional network for light field saliency detection. In particular, we observe that the proposed approach shows significant performance gains when compared to previous methods on the proposed dataset for all metrics. The performance is decreased on the HFUT-Lytro and LFSD datasets, which is owing to the limited viewpoint information in these datasets. Therefore, a large number of filters learnt on the proposed dataset are significantly underused during generalization. This

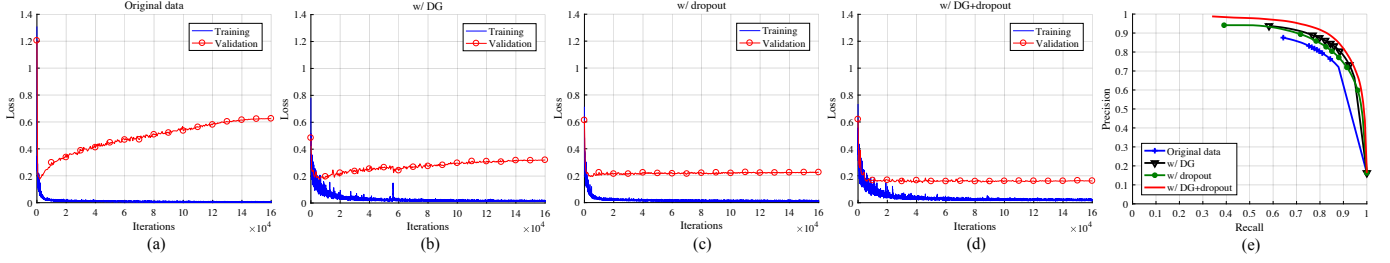


Fig. 12. Training and validation loss for LFNet-9 × 9 on the proposed Lytro Illum dataset. (a) Original training data. (b) Training with DG. (c) Training with dropout. (d) Training with DG and dropout. (e) PR curves for different strategies.

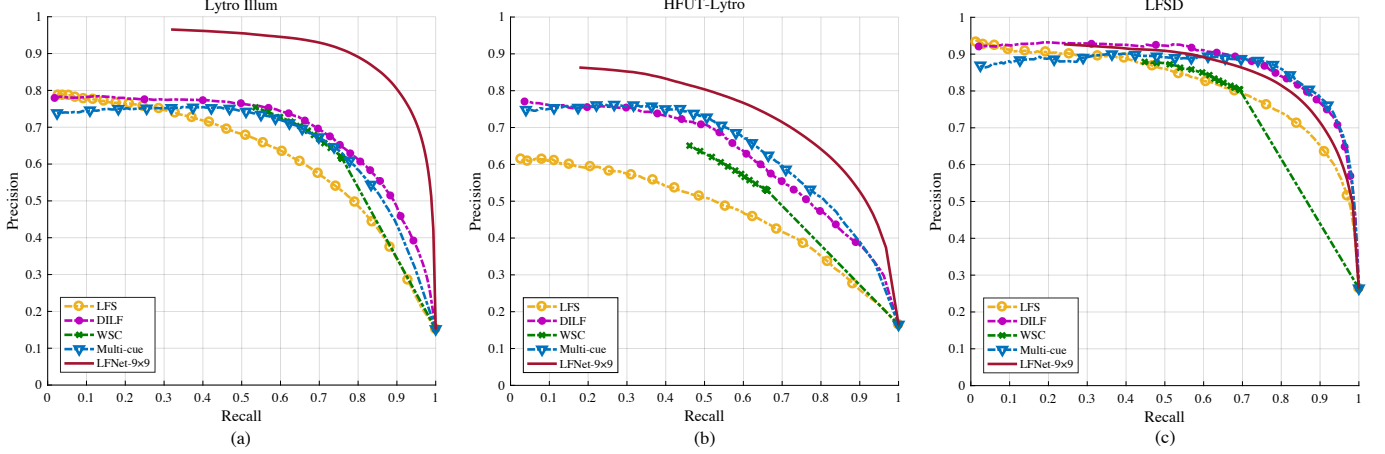


Fig. 13. Comparison on three datasets in terms of PR curve. (a) The proposed Lytro Illum dataset. (b) HFUT-Lytro dataset. (c) LFSD dataset.

demonstrates that different light field datasets do affect the accuracy of methods. Multi-cue [2] and DILF [20] methods show better performance than our approach in terms of F-measure and AP on the LFSD dataset. The reason is that these methods use external depth features and post-processing refinement to improve the performance.

Some qualitative results are shown in Figure 14. We can see that our approach can handle various challenging scenarios, including multiple salient objects (rows 1 and 2), highly cluttered backgrounds (rows 3 and 5), small salient objects (rows 4 and 7), inconsistent illumination (rows 1 and 6), and salient objects in similar backgrounds (rows 8, 9 and 10). It is also worth noting that without any post-processing methods, our approach can highlight salient objects more uniformly than other methods.

## VI. CONCLUSION

This paper introduces a deep convolutional network for saliency detection on light fields by exploiting multi-view information in micro-lens images. Specifically, we propose LFNet variants to process the micro-lens image array. This paper can be viewed as the first work that addresses light field saliency detection using an end-to-end CNN. To facilitate training such a deep network, we introduce a challenging saliency dataset with light field images captured from a Lytro Illum camera. In total, 640 high quality light fields are produced, making the dataset the largest among existing light field saliency datasets. Extensive experiments demonstrate that

comparing to 2D saliency, 4D light field saliency can learn additional angular information contributing to increase the performance of saliency detection. The proposed network outperforms the state-of-the-art methods on the proposed dataset and generalizes well to the existing datasets. In particular, our approach is capable of detecting salient regions in challenging cases, such as the similar salient foreground and background, inconsistent illuminant, multiple salient objects, and cluttered background. Our work suggests promising future directions of exploiting spatial and angular patterns in light fields and deep learning technologies to advance the state-of-the-art in pixel-wise prediction tasks.

## REFERENCES

- [1] N. Li, J. Ye, Y. Ji, H. Ling, and J. Yu, “Saliency detection on light field,” in *IEEE Conference on Computer Vision and Pattern Recognition*, 2014. 1, 2, 3, 5, 8, 10
- [2] J. Zhang, M. Wang, L. Lin, X. Yang, J. Gao, and Y. Rui, “Saliency detection on light field: A multi-cue approach,” *ACM Transactions on Multimedia Computing, Communications, and Applications*, vol. 13, no. 3, 2017. 1, 2, 3, 5, 8, 9, 10
- [3] E. H. Adelson and J. Y. Wang, “Single lens stereo with a plenoptic camera,” *IEEE Transactions on Pattern Analysis and Machine Intelligence*, vol. 14, no. 2, pp. 99–106, 1992. 1
- [4] S. Wanner and B. Goldluecke, “Globally consistent depth labeling of 4d light fields,” in *IEEE Conference on Computer Vision and Pattern Recognition*, 2012, pp. 41–48. 1
- [5] “Lytro, inc.” <https://www.lytro.com/>. 1
- [6] “Raytrix gmbh,” <https://raytrix.de/>. 1
- [7] M. Levoy and P. Hanrahan, “Light field rendering,” in *Computer graphics and interactive techniques*, 1996, pp. 31–42. 1, 3, 8

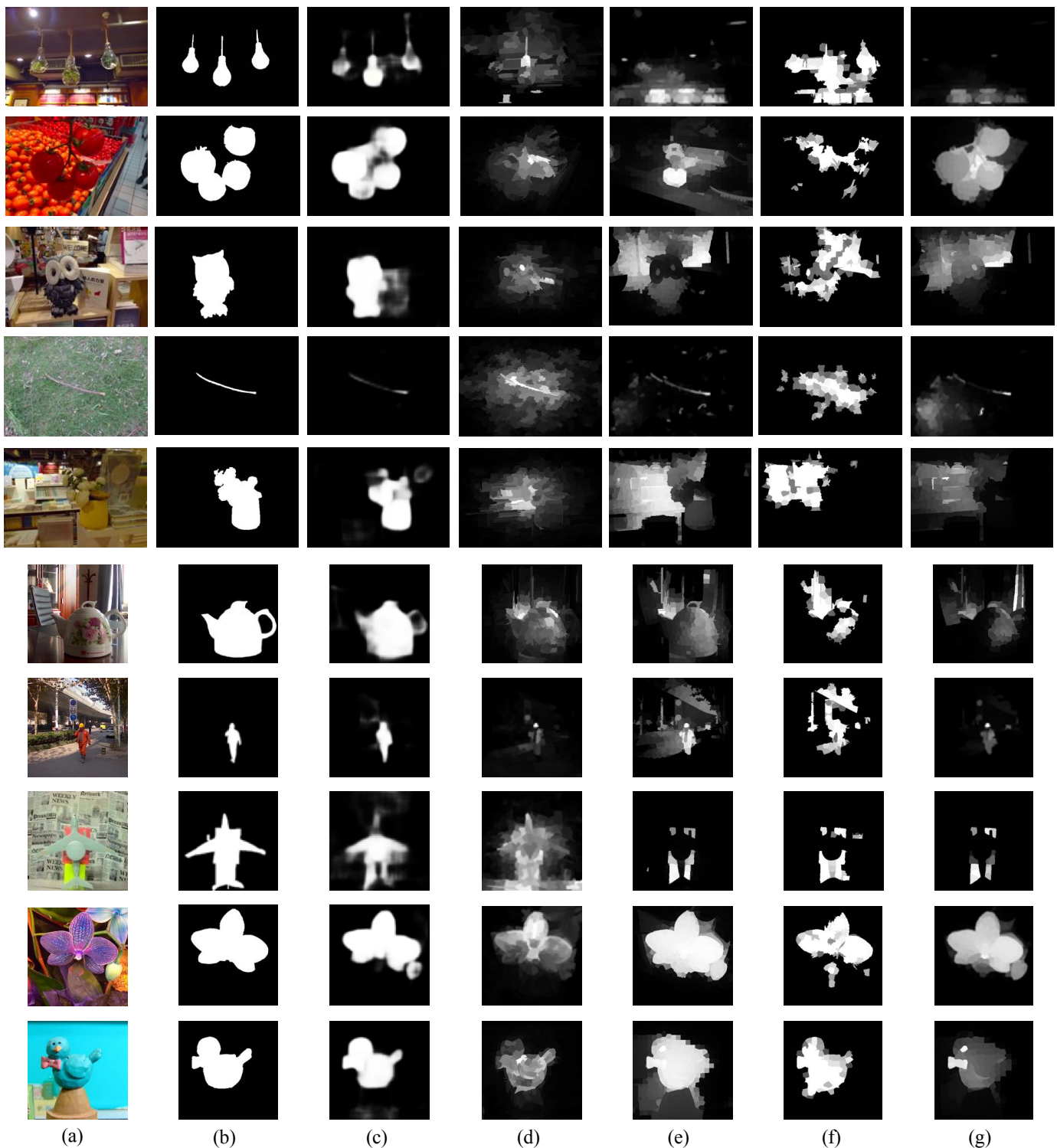


Fig. 14. Visual comparison of our best LFNet variant (LFNet- $9 \times 9$ ) and other state-of-the-art methods on three datasets. (a) Central viewing images. (b) Ground-truth maps. (c) LFNet- $9 \times 9$ . (d) LFS [1]. (e) DILF [20]. (f) WSC [21]. (g) Multi-cue [2]. The first five samples are taken from the proposed Lytro Illum dataset, the middle three samples are taken from the HFUT-Lytro dataset, and the last two samples are taken from the LFSD dataset.

- [8] R. Ng, M. Levoy, M. Brédif, G. Duval, M. Horowitz, and P. Hanrahan, “Light field photography with a hand-held plenoptic camera,” Stanford University Computer Science, Technical Report, 2005. **1**
- [9] S. Wanner and B. G. and, “Variational light field analysis for disparity estimation and super-resolution,” *IEEE Transactions on Pattern Analysis and Machine Intelligence*, vol. 36, no. 3, pp. 606–619, 2014. **1**
- [10] T.-C. Wang, J.-Y. Zhu, and E. Hiroaki, “A 4D light-field dataset and CNN architectures for material recognition,” in *European Conference on Computer Vision*, 2016. **1**
- [11] R. Raghavendra, K. B. Raja, and C. Busch, “Presentation attack detection for face recognition using light field camera,” *IEEE Transactions on Image Processing*, vol. 24, no. 3, pp. 1060–1075, 2015. **1**
- [12] A. Sepas-Moghaddam, M. A. Haque, P. L. Correia, K. Nasrollahi, T. B. Moeslund, and F. Pereira, “A double-deep spatio-angular learning



- framework for light field based face recognition,” arXiv:1805.10078v2, 2018. 1
- [13] M. W. Tao, P. P. Srinivasan, and S. Hadap, “Shape estimation from shading, defocus, and correspondence using light-field angular coherence,” *IEEE Transactions on Pattern Analysis and Machine Intelligence*, vol. 39, no. 3, pp. 546–560, 2017. 1
  - [14] W. Williem, I. K. Park, and K. M. Lee, “Robust light field depth estimation using occlusion-noise aware data costs,” *IEEE Transactions on Pattern Analysis and Machine Intelligence*, p. 10.1109/TPAMI.2017.2746858, 2017. 1
  - [15] C. Shin, H.-G. Jeon, Y. Yoon, I. S. Kweon, and S. J. Kim, “EPINET: A fully-convolutional neural network using epipolar geometry for depth from light field images,” in *IEEE Conference on Computer Vision and Pattern Recognition*, 2018. 1, 5
  - [16] H. Schilling, M. Diebold, C. Rother, and B. Jähne, “Trust your model: Light field depth estimation with inline occlusion handling,” in *IEEE Conference on Computer Vision and Pattern Recognition*, 2018, pp. 4530–4538. 1
  - [17] H.-G. Jeon, J. Park, G. Choe, J. Park, Y. Bok, Y. W. Tai, and I. S. Kweon, “Depth from a light field image with learning-based matching costs,” *IEEE Transactions on Pattern Analysis and Machine Intelligence*, vol. 10.1109/TPAMI.2018.2794979, 2018. 1
  - [18] Y. Yoon, H.-G. Jeon, and D. Yoo, “Learning a deep convolutional network for light-field image super-resolution,” in *IEEE International Conference on Computer Vision Workshop*, 2015. 1
  - [19] G. Wu, Y. Liu, L. Fang, Q. Dai, and T. Chai, “Light field reconstruction using convolutional network on epi and extended applications,” *IEEE Transactions on Pattern Analysis and Machine Intelligence*, vol. 10.1109/TPAMI.2018.2845393, 2018. 1
  - [20] J. Zhang, M. Wang, J. Gao, Y. Wang, X. Zhang, and X. Wu, “Saliency detection with a deeper investigation of light field,” in *International Joint Conference on Artificial Intelligence*, 2015, pp. 2212–2218. 1, 3, 8, 9, 10
  - [21] N. Li, B. Sun, and J. Yu, “A weighted sparse coding framework for saliency detection,” in *IEEE Conference on Computer Vision and Pattern Recognition*, 2015. 1, 3, 8, 10
  - [22] L. Wang, H. Lu, X. Ruan, and M.-H. Yang, “Deep networks for saliency detection via local estimation and global search,” in *IEEE Conference on Computer Vision and Pattern Recognition*, 2015, pp. 3183–3192. 1, 3
  - [23] G. Li and Y. Yu, “Visual saliency based on multiscale deep features,” in *IEEE Conference on Computer Vision and Pattern Recognition*, 2015. 1, 3
  - [24] R. Zhao, W. Ouyang, H. Li, and X. Wang, “Saliency detection by multi-context deep learning,” in *IEEE Conference on Computer Vision and Pattern Recognition*, 2015. 1, 3
  - [25] N. Liu, J. Han, and M.-H. Yang, “PiCANet: Learning pixel-wise contextual attention for saliency detection,” in *IEEE Conference on Computer Vision and Pattern Recognition*, 2018. 1, 3
  - [26] J. Kuen, Z. Wang, and G. Wang, “Recurrent attentional networks for saliency detection,” in *IEEE Conference on Computer Vision and Pattern Recognition*, 2016. 1, 3
  - [27] X. Zhang, T. Wang, J. Qi, H. Lu, and G. Wang, “Progressive attention guided recurrent network for salient object detection,” in *IEEE Conference on Computer Vision and Pattern Recognition*, 2018. 1, 3
  - [28] L. Wang, L. Wang, H. Lu, P. Zhang, and X. Ruan, “Saliency detection with recurrent fully convolutional networks,” in *European Conference on Computer Vision*, 2016, pp. 825–841. 1, 3
  - [29] Y. Niu, Y. Geng, X. Li, and F. Liu, “Leveraging stereopsis for saliency analysis,” in *IEEE Conference on Computer Vision and Pattern Recognition*, 2012, pp. 454–461. 1
  - [30] V. Sitzmann, A. Serrano, A. Pavel, M. Agrawala, D. Gutierrez, B. Masia, and G. Wetzstein, “Saliency in VR: How do people explore virtual environments?” *IEEE transactions on visualization and computer graphics*, vol. 24, no. 4, pp. 1633–1642, 2018. 1
  - [31] R. Achanta, S. Hemami, F. Estrada, and S. Susstrunk, “Frequency-tuned salient region detection,” in *IEEE Conference on Computer Vision and Pattern Recognition*, 2009, pp. 1597–1604. 2, 6
  - [32] C. Yang, L. Zhang, H. Lu, X. Ruan, and M.-H. Yang, “Saliency detection via graph-based manifold ranking,” in *IEEE Conference on Computer Vision and Pattern Recognition*, 2013, pp. 3166–3173. 2
  - [33] Y. Li, X. Hou, C. Koch, J. M. Rehg, and A. L. Yuille, “The secrets of salient object segmentation,” in *IEEE Conference on Computer Vision and Pattern Recognition*, 2014, pp. 280–287. 2
  - [34] L. C. Chen, G. Papandreou, I. Kokkinos, K. Murphy, and A. L. Yuille, “DeepLab: Semantic image segmentation with deep convolutional nets, atrous convolution, and fully connected crfs,” *IEEE Transactions on Pattern Analysis and Machine Intelligence*, vol. 40, no. 4, pp. 834–848, 2018. 2, 4, 5
  - [35] D. G. Dansereau, O. Pizarro, and S. B. Williams, “Decoding, calibration and rectification for lenselet-based plenoptic cameras,” in *IEEE Conference on Computer Vision and Pattern Recognition*, 2013, pp. 1027–1034. 3
  - [36] O. Russakovsky, J. Deng, H. Su, J. Krause, S. Satheesh, S. Ma, Z. Huang, A. Karpathy, A. Khosla, M. Bernstein, A. C. Berg, and L. Fei-Fei, “Imagenet large scale visual recognition challenge,” *International Journal of Computer Vision*, vol. 115, no. 3, pp. 211–252, 2015. 3
  - [37] K. Simonyan and A. Zisserman, “Very deep convolutional networks for large-scale image recognition,” arXiv:1409.1556, 2014. 3, 4
  - [38] G. Li and Y. Yu, “Deep contrast learning for salient object detection,” in *IEEE Conference on Computer Vision and Pattern Recognition*, 2016. 3
  - [39] S. S. S. Kruthiventi, V. Gudisa, J. H. Dholakiya, and R. V. Babu, “Saliency unified: A deep architecture for simultaneous eye fixation prediction and salient object segmentation,” in *IEEE Conference on Computer Vision and Pattern Recognition*, 2016. 3
  - [40] L. McMillan and G. Bishop, “Plenoptic modeling: An image-based rendering system,” in *Computer graphics and interactive techniques*, 1995, pp. 39–46. 3
  - [41] E. H. Adelson and J. R. Bergen, “The plenoptic function and the elements of early vision,” in *Computational Models of Visual Processing*. The MIT Press, 1991. 3
  - [42] H. Tang and K. N. Kutulakos, “What does an aberrated photo tell us about the lens and the scene?” in *IEEE International Conference on Computational Photography*, 2013, pp. 1–10. 3
  - [43] H.-G. Jeon, J. Park, G. Choe, J. Park, Y. Bok, Y.-W. Tai, and I. S. Kweon, “Accurate depth map estimation from a lenslet light field camera,” in *IEEE Conference on Computer Vision and Pattern Recognition*, 2015, pp. 1547–1555. 3
  - [44] S. Zhang, H. Sheng, D. Yang, J. Zhang, and Z. Xiong, “Micro-lens-based matching for scene recovery in lenslet cameras,” *IEEE Transactions on Image Processing*, vol. 27, no. 3, pp. 1060–1075, 2018. 3
  - [45] “Lytro Power Tools,” <https://github.com/kmader/lytro-power-tools>. 3
  - [46] E. Shelhamer, J. Long, and T. Darrell, “Fully convolutional networks for semantic segmentation,” *IEEE Transactions on Pattern Analysis and Machine Intelligence*, vol. 39, no. 4, pp. 640–651, 2017. 4
  - [47] L.-C. Chen, G. Papandreou, I. Kokkinos, K. Murphy, and A. L. Yuille, “Semantic image segmentation with deep convolutional nets and fully connected crfs,” arXiv:1412.7062v4, 2016. 4
  - [48] C. Szegedy, V. Vanhoucke, S. Ioffe, J. Shlens, and Z. Wojna, “Rethinking the inception architecture for computer vision,” in *IEEE Conference on Computer Vision and Pattern Recognition*, 2016, pp. 2818–2826. 4
  - [49] L.-C. Chen, Y. Zhu, G. Papandreou, F. Schroff, and H. Adam, “Encoder-decoder with atrous separable convolution for semantic image segmentation,” arXiv preprint arXiv:1802.02611, 2018. 4
  - [50] M. Streche, A. Alperovich, and B. Goldluecke, “Accurate depth and normal maps from occlusion-aware focal stack symmetry,” in *IEEE Conference on Computer Vision and Pattern Recognition*, 2017, pp. 2529–2537. 5
  - [51] Y. Jia, E. Shelhamer, J. Donahue, S. Karayev, J. Long, R. Girshick, S. Guadarrama, and T. Darrell, “Caffe: Convolutional architecture for fast feature embedding,” arXiv preprint arXiv:1408.5093, 2014. 5
  - [52] M. Everingham, S. A. Eslami, L. V. Gool, C. K. Williams, J. Winn, and A. Zisserman, “The pascal visual object classes challenge: A retrospective,” *International Journal of Computer Vision*, vol. 111, no. 1, pp. 98–136, 2014. 5
  - [53] X. Glorot and Y. Bengio, “Understanding the difficulty of training deep feedforward neural networks,” in *International Conference on Artificial Intelligence and Statistics*, 2010, pp. 249–256. 5
  - [54] R. Margolin, L. Zelnik-Manor, and A. Tal, “How to evaluate foreground maps,” in *IEEE Conference on Computer Vision and Pattern Recognition*, 2014. 6
  - [55] M. Levoy, Z. Zhang, and I. McDowall, “Recording and controlling the 4d light field in a microscope using microlens arrays,” *Journal of microscopy*, vol. 235, no. 2, pp. 144–162, 2009. 7
  - [56] M. L. Pendu, X. Jiang, and C. Guillemot, “Light field inpainting propagation via low rank matrix completion,” *IEEE Transactions on Image Processing*, vol. 27, no. 4, pp. 1981–1993, 2018. 8